lubricants

MDPI

Article

How Electrical Arcing Governs Wear and Performance in Current-Carrying Pantograph Contacts

Yanjiao Nie [1], Jinhao Shao [1], Li Xiao [2], Wenhao Dai [2], Dehui Ji [2,*] and Limei Kang [1,3,*]

[1] Science and Technology Industry Division, Guangzhou Railway Polytechnic, Zengcheng District Science and Education City Campus, Guangzhou 511300, China
[2] Key Laboratory of Transportation Intelligent Operation and Maintenance Technology and Equipment, Ministry of Education, East China Jiaotong University, Nanchang 330013, China
[3] National Engineering Research Center of Near-Net-Shape Forming for Metallic Materials, South China University of Technology, Guangzhou 510640, China
* Correspondence: jidehui_1990@163.com (D.J.); kanglimei@gtxy.edu.cn (L.K.)

Abstract

The pantograph–catenary system serves as the core power supply device, ensuring stable operation of high-speed trains, and its contact interface represents a typical current-carrying friction system, where the introduction of electric current significantly complicates the wear mechanisms. The coupling effect of mechanical wear and electrical wear exacerbates damage to and degradation of carbon strip materials, while electric arcs induced by unstable contact states directly regulate the tribological characteristics and electrical conductivity of the friction pair. To investigate the current-carrying friction and wear behavior of carbon strips under the dominant effect of electric arcs, this study simulated the irregularity conditions of contact wires, observed the evolution characteristics of electric arcs, and systematically analyzed the effects of test current and contact load on the damage characteristics and current-carrying performance of the contact pair. The results indicate that arc morphology exhibits differentiated characteristics across friction cycles, with significant fluctuations in arc intensity. Regarding the friction coefficient, under a contact load of 25 N, the friction coefficients corresponding to currents of 0 A, 40 A, and 80 A are 0.378, 0.242, and 0.335, respectively; under a contact load of 50 N, the corresponding values are 0.432, 0.180, and 0.209, respectively. The friction coefficients under current-free conditions are consistently higher than those under current-carrying conditions. In terms of wear rate, under a contact load of 25 N, the wear rates at 0 A, 40 A, and 80 A are 0.0069, 0.299, and 2.70 $mm^3/(N{\cdot}m)$, respectively; under a contact load of 50 N, they are 0.010, 0.133, and 1.133 $mm^3/(N{\cdot}m)$, respectively. No positive correlation is observed between contact load and the wear rate of the carbon-based friction pair, whereas increasing test current significantly exacerbates material damage. Regarding contact resistance, under a contact load of 25 N, the contact resistances at 40 A and 80 A are 34.7 Ω and 46.6 Ω, respectively; under a contact load of 50 N, they are 27.7 Ω and 37.9 Ω, respectively, indicating that lower contact loads correspond to higher contact resistances, and higher test currents also result in higher contact resistances. In summary, both increasing current and decreasing contact load aggravate the electrical damage to the contact pair materials, while increasing contact load exerts a significant inhibitory effect on electrical damage. This study provides theoretical insights into the damage mechanism and arc morphology evolution laws induced by electric arcs under contact wire irregularity conditions.

Keywords: bow-and-net system; current-induced friction; contact load; current intensity; damage mechanism

Check for updates

Received: 28 July 2026
Revised: 14 September 2026
Accepted: 22 September 2026
Published: 28 September 2026

Copyright: © 2026 by the authors. Licensee MDPI, Basel, Switzerland. This article is an open access article distributed under the terms and conditions of the Creative Commons Attribution (CC BY) license.

1. Introduction

The pantograph contact system serves as the primary power source for high-speed trains, playing a vital role in ensuring their safe and stable operation. This system consists of pantograph carbon sliding plates and contact wires. The pantograph collector is mounted on the locomotive's roof and operates simultaneously with the locomotive; under load, it extracts electrical energy from the contact wire through sliding friction [1].

However, the complex operating conditions of trains frequently induce severe mechanical and electrical wear on carbon sliding plates, and frequent arc formation is one of the common faults in the pantograph system. Mechanical and electrical wear create a vicious cycle on wear surfaces [2], significantly degrading the performance of contact materials. Liu et al. [3] found that electric current induces surface oxidation and spalling, with both wear rates and oxidation levels showing direct proportional relationships to current intensity. Wear mechanisms vary under different currents: under a strong 160 A current, oxidative and delamination wear dominate; when the current decreases to 80 A or below, abrasive and adhesive wear become predominant [4]. Additionally, due to the dynamic characteristics of high-speed sliding in pantograph systems, contact instability cannot be entirely avoided. This instability arises from vehicle vibrations, irregular contact lines, airflow disturbances, and localized defects at contact surfaces, further triggering arc formation [5–7]. Arc discharge energy shows a positive correlation with the total wear depth of carbon plates [8]; arc generation accumulates energy and raises temperatures between friction pairs, exacerbating surface electrical wear [9], while eroded contact surfaces promote subsequent arc discharge, creating a self-reinforcing cycle. Yang et al. [10] concluded that severe arc erosion leads to delamination, initially occurring at the edges of large erosion pits before spreading and ultimately causing significant material damage through combined electrical and mechanical wear effects.

Furthermore, the electrical performance of the system is a key focus for researchers. Only when the system meets criteria such as high current-carrying efficiency, low current-carrying fluctuation, and appropriate contact resistance can trains operate stably at high speeds. Researchers have found that parameters including the contact wire center distance [11], carbon slipper material [12], and load [13] significantly influence the contact resistance of the friction pair, with this resistance increasing progressively as the sliding distance increases. Hu et al. [12] concluded that the presence of a "copper network structure" in carbon slippers helps maintain low resistivity and high wear resistance. Additionally, the system's electrical performance is severely affected by arc phenomena: Hu et al. [9] observed significant current distortion during high-speed operation of the contact pair, accompanied by "zero-current" regions indicative of arc discharge [14]. Zhang et al. [15] identified 80 km/h as the inflection point for both arc rate and current-carrying efficiency; beyond this speed, the arc rate rises sharply while current-carrying efficiency declines dramatically, leading to a deterioration in system performance.

The rapid deterioration or even failure of materials caused by electric arcs in catenary systems due to vibration and other factors remains a significant challenge for high-speed trains [16]. While extensive research has been conducted on catenary arcs, most studies have focused on the relationship between arcs and material damage [17]. To systematically investigate the morphological evolution of arcs under varying intensities and their impacts on material friction-wear performance and electrical properties, this experiment simulated arc phenomena induced by vibration by creating irregularities on copper discs. The study specifically analyzed how current and load variations influence material friction-wear behavior and electrical transmission characteristics, thereby providing insights into the wear mechanisms of carbon sliding plates and the evolution of catenary electrical performance under arc effects and uneven operating conditions.

2. Materials and Methods

2.1. Test Equipment and Materials

The experimental tests of certain equipment and materials were conducted using a disc-type current-carrying friction and wear tester, as shown in Figure 1a. The carbon pin, fabricated from carbon sliding plates used in high-speed railways, served as the upper specimen, while the copper disc, made of pure copper (99.9%), served as the lower specimen; the current-carrying friction between the carbon pin and the copper disc simulated the electrical sliding contact between the carbon sliding plate and the contact wire. The chemical composition of the carbon pin is as follows: C constitutes 84.45 wt%, O constitutes 10.2 wt%, and elements such as S, P, and Cl account for a combined 5.35 wt%. The schematic diagram of the current-carrying circuit is shown in Figure 1b, which comprises a voltage stabilizer, resistors, a carbon pin, a copper disc, and numerous conductors; current and voltage sensors monitor the current and voltage at the contact pair in real time, with the data acquisition system transmitting the measurements to a computer.

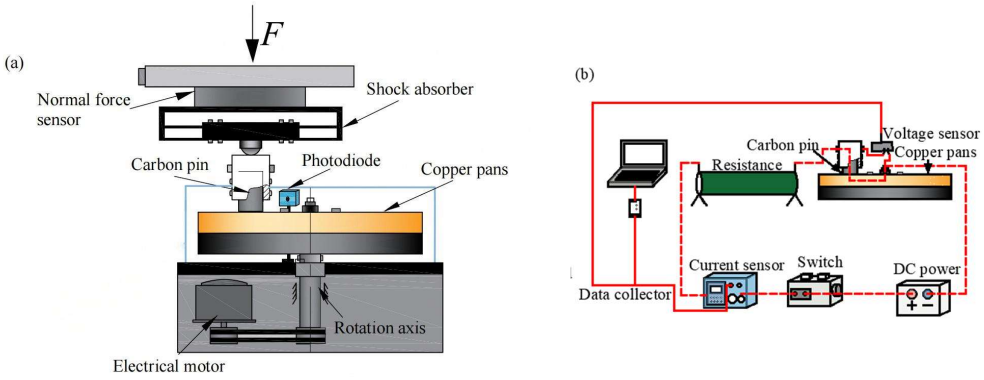


Figure 1. Pin-on-disc tribometer for current-carrying friction and wear testing. (**a**) Schematic diagram of the testing machine; (**b**) test circuit diagram.

2.2. Test Procedure and Methods

Prior to commencing the test, to ensure optimal contact between the carbon pin and the copper disc, the surface of the copper disc was sequentially ground using sandpaper grades 100#, 600#, 1000#, 1200#, and 2000#. The copper disc was leveled using a micrometer with a resolution of 0.0005 mm (model Sanliang 312-831, Dongguan Sanliang Measuring Tools Co., Ltd., Dongguan, China), and a contact load of 30 N was applied to pre-grind the contact surface until the contact area exceeded 80%. Subsequently, four points (1, 2, 3, 4) were marked at equally spaced intervals on the copper disc; the surface roughness at point 4 was adjusted to 0.4 mm to simulate the actual roughness conditions under operating conditions, as shown in Figure 2.

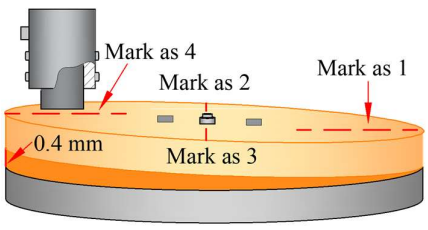


Figure 2. Method for setting the unevenness of the copper disc.

To investigate the effects of load and current on arc and sliding friction damage, two variables were established in the experiment: contact load and current magnitude. The load F_n (N) was set at 25 and 50, while the test current I (A) was set at 0, 40, and 80.

Other parameters included copper disc rotation speed v (Hz): 1; friction radius R (mm): 82; and experimental duration T (s): 1800. During the experiments, a Canon EOS R100 camera (i-SPEED 717, iX Cameras Ltd., Rochford, UK). was used to record the friction characteristics of the contact pair and the arc morphology. Experiments with identical parameters were repeated at least three times to ensure reliable results.

2.3. Data Processing for Experimental Tests

(1) Friction coefficient and wear rate: Data processing for test (1) friction coefficient and wear rate: Throughout the friction test, tangential and normal forces are measured in real time using two-dimensional tangential and normal force sensors. The instantaneous friction coefficient (μ_i) is calculated by dividing the measured real-time tangential force by the applied normal load. The average friction coefficient (μ_a) is computed as shown in Equation (1):

$$\mu_a = \frac{1}{t}\int_0^t \mu_i dt \tag{1}$$

In the formula, t is the friction time (s).

We used an electronic balance with a precision of 0.1 mg to weigh the carbon pins before and after the test, repeating the measurement eight times and taking the average value. The weight before the test was denoted as m_0, and the weight after the test was denoted as m_1; the wear rate was calculated using Equation (2).

$$w = \frac{m_0 - m_1}{L}; w_V = \frac{w}{\rho \cdot F_N} \times 1000 \tag{2}$$

In the formula, w represents the quality wear rate (g/km), and L denotes the relative sliding distance between the contact pairs (km); w_V represents the specific volumetric wear rate ($mm^3/(N \cdot m)$); ρ denotes the density value. ρ = 1.66 g/cm^3.

(2) Contact resistance and arc energy: Contact resistance is one of the key parameters characterizing electrical contact performance, and its value is closely related to the contact state of the friction pair. By using a data acquisition device to record the voltage drop and circuit current of the contact pair in real time, the average contact resistance is calculated using Equation (3). The term "contact resistance" mentioned herein refers to the average value measured when the contact pair is in contact.

$$R = \frac{1}{n}\sum_i^n \frac{U_i}{I_i} \tag{3}$$

In the formula, R represents the average contact resistance (mΩ); U_i denotes the real-time voltage drop at the carbon/copper contact interface (V); and I_i indicates the real-time current in the circuit under contact conditions (A).

In current-carrying friction tests, arc discharge energy represents a quantitative measure of arc discharge intensity, which is closely related to factors such as the number of arc discharges and discharge duration during the test. The arc discharge energy per unit distance is calculated using Equation (4).

$$E = \frac{\int U_i I_i dt}{L} \tag{4}$$

In the formula, E represents the average arc discharge energy per unit distance (kJ/km); Ui denotes the real-time voltage drop at the carbon/copper contact interface (V); I_i indicates the real-time current in the circuit (A); and L is the relative sliding distance between the contact interfaces (km).

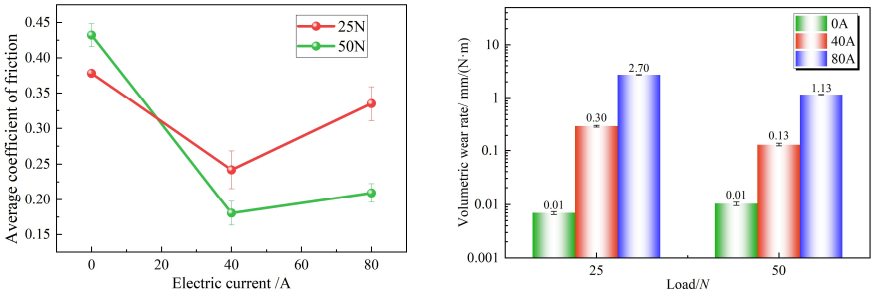
2.4. Characterization Analysis

Characterization analysis was performed using a three-dimensional profilometer ((Zygo, ZeGageTM Pro HR, Zygo Corporation, Middlefield, CT, USA)) to examine the wear regions at position 3 of the carbon pin and copper disc post-test, including the three-dimensional morphology of wear marks and surface roughness. The macroscopic morphology of both the carbon pin and copper disc was captured using a high-definition SAIKEDIGITAL camera (Zoom lens 2 07150282, iX Cameras Ltd., Rochford, UK). Microscopic morphology and elemental distribution of the carbon pin's wear regions were analyzed employing an electron microscope (SEM; HITACHI SU8010, Hitachi, Japan) and an energy-dispersive spectrometer (EDS; X-Flash 6I60, Bruker, Billerica, MA, USA).

3. Results

3.1. Frictional Characteristics of Carbon/Copper Friction Pairs

The friction characteristics of the carbon/copper friction pair under contact loads of 25 N and 50 N, as well as their friction coefficients and wear rates at different current intensities (0 A, 40 A, and 80 A), are shown in Figure 3. Under various contact load conditions (Figure 3a), the friction coefficient in the no-current scenario was significantly higher than that in the current-carrying scenario; moreover, the friction coefficient at 80 A exceeded that at 40 A. In the no-current condition, the average friction coefficient at 50 N was markedly higher than that at 25 N. Increased contact load enhances the adhesion between micro-relief structures on material surfaces, thereby increasing cutting forces and, consequently, the friction coefficient [18]. Compared to the volumetric wear rate of carbon (Figure 3b), the volumetric wear rate of the carbon pin under a 50 N load in the no-current operating condition (0.01 mm/(N·m)) is approximately equivalent to 25 N (0.01 mm/(N·m)). When the current is increased to 40 A, the volumetric wear rate for a carbon pin subjected to a 25 N load (0.30 mm/(N·m)) is approximately 2.3 times that observed for a 50 N load (0.13 mm/(N·m)). However, under an 80 A operating condition with a contact load of 25 N, the volumetric wear rate of the carbon pin (2.7 mm/(N·m)) is approximately 139% higher than that under the 50 N operating condition (1.13 mm/(N·m)). Furthermore, under all loading conditions, the volumetric wear rate of the carbon pin shows an increasing trend as the current increases; in particular, the volumetric wear rate at 80 A is approximately nine times higher than that at 40 A. This indicates that there is no positive correlation between the load and the volumetric wear rate of the carbon friction pair, whereas an increase in current significantly exacerbates the wear damage to the carbon friction pair. Under a 40 A current condition, increasing the contact load reduces the wear rate; under an 80 A current condition, increasing the contact load also reduces the wear rate. It can be observed that, under the current operating conditions, the wear rate of the carbon friction pair is negatively correlated with the contact load.



(**a**) Average friction coefficient (**b**) Volumetric wear rate

Figure 3. COF and volumetric wear rate of carbon/copper tribo-pair under two types of contact loads at different currents.

Under low-load conditions (25 N), intermittent separation between the carbon pin and copper disc occurs due to surface irregularities, inevitably leading to arc formation. Under high-load conditions, stable contact between the components prevents significant arc formation; thus, only arc characteristics at 25 N were recorded. Figure 4 shows typical arc patterns captured at identical positions during cycles 0–400, 400–800, 800–1200, and 1200–1600. Comparison reveals that arc intensity at 40 A is significantly lower than at 80 A, with values during the first 800 cycles Figure 4(a-0,a-1) exceeding those after cycle 800 Figure 4(a-2,a-3). The highest arc intensity appears during the initial friction phase of the first 400 cycles, exhibiting flame-shaped bright spots accompanied by arc-pulling phenomena (Figure 4(a-0)). During this period, the contact pair remains in an adaptation phase, resulting in intense arc generation. After the completion of the adaptation phase, reduced micro-protrusions allow early carbon wear debris to fill interstitial gaps, providing a lubricating effect and leading to a decline in arc intensity post-cycle 800 (Figure 4(a-2,a-3)). In contrast, under 80 A conditions, nearly all arcs throughout the cycle exhibit substantial intensity with a vigorous glow during the adaptation phase (Figure 4(b-0)), while arc intensity slightly decreases during cycles 400–800, resembling the initial arc pattern observed at 40 A (Figure 4(b-1)). Subsequently, the arc intensity increases (Figure 4(b-2)), reaching its peak during the final stage of friction (1200–1600 cycles) (Figure 4(b-3)). This is attributed to prolonged arc erosion causing persistent cumulative damage to the contacting materials, leading to significant deterioration of the contact surface; this degradation further triggers more frequent arc phenomena, creating a positive feedback loop. This interaction progressively intensifies, ultimately resulting in substantial performance degradation of the material under an 80 A current condition.

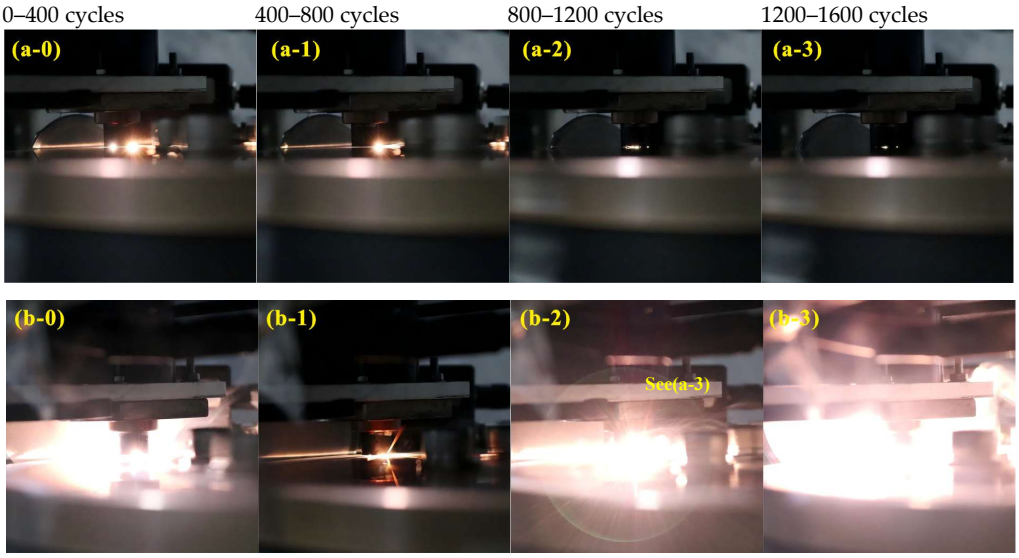


Figure 4. Arc shapes at different cycle numbers under 25N condition: 40A, 0–400 cycles (**a-0**); 40A, 400–800 cycles (**a-1**); 40A, 800–1200 cycles (**a-2**); 40A, 1200–1600 cycles (**a-3**); 80A, 0–400 cycles (**b-0**); 80A, 400–800 cycles (**b-1**); 80A, 8–1200 cycles (**b-2**); 80A, 1200–1600 cycles (**b-3**).

During current-carrying friction processes, intense arc discharges can temporarily distort the current waveform [19]. Figure 5 illustrates the evolution of actual current waveforms passing through the contact pair under different loads. Under a 25 N load condition, the 40 A current exhibits a regular quasi-sinusoidal curve; however, when the current is increased to 80 A, the waveform becomes irregular. Upon locally magnifying a specific region of the current waveform (Figure 5c), it is observed that the arc discharge phenomenon occurring under condition A causes distortion of the current waveform. This includes the fact that the current does not exhibit a sinusoidal waveform, as well as the

inconsistent duration during which the current is zero A [20]. A comparison between curves at 50 N (Figure 5d) and 25 N shows that currents under the latter condition fluctuate around a steady level. This stability arises because high-load conditions maintain close contact between friction pairs, eliminating arc generation and thus preventing current disturbance.

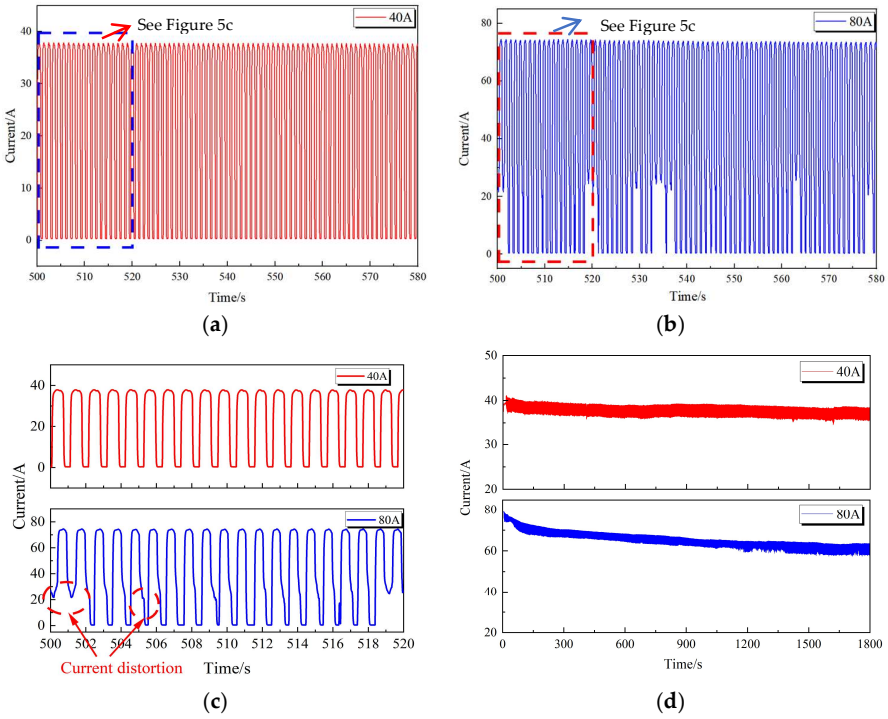


Figure 5. Current variation under two types of contact loads. (**a**) Current variation for 25 N and 40 A; (**b**) current variation for 25 N and 80 A; (**c**) 25 N, local variation in current; (**d**) current variations for 50 N, 40 A, and 80 A.

During electrical contact friction, contact resistance primarily consists of contraction resistance and film resistance [21]. The value of contraction resistance depends on the number and size of surface micro-relief features (i.e., conductive spots), exhibiting an inverse relationship with their quantity. Film resistance arises from a layer of poorly conductive material (including oxide films and other contaminants) present on the contact surfaces. Thus, contact resistance directly correlates with the contact condition of the pair. Figure 6a shows the average contact resistances at current levels of 40 A and 80 A under different contact loads. A comparison reveals that an 80 A current consistently yields higher contact resistances than a 40 A current. When an 80 A current flows through the contact pair, both Joule heat and arc heat generation are significantly greater than at 40 A; these elevated temperatures rapidly promote oxide formation on contact surfaces. Oxides exhibit poor conductivity [22], while arc ablation causes severe damage to worn surfaces, reducing the effective contact area and, consequently, increasing contact resistance between friction pairs.

Furthermore, at the same current intensity, the contact resistance under a contact load of 50 N is lower than that at 25 N. In the absence of external interference, increasing the contact load helps reduce arc formation; optimal contact conditions effectively increase both the contact area and the number of contact spots, thereby lowering the contact resistance [23]. Figure 6b shows the arc discharge energy per unit distance under different contact loads at current levels of 40 A and 80 A. At identical contact loads, the arc discharge energy at 80 A is approximately four times that at 40 A. According to the calculation formula for arc discharge energy, this value exhibits a positive correlation with current intensity, meaning

it increases with rising current. When the contact load increases to 50 N, the arc discharge energy decreases compared to low-load conditions; specifically, the arc discharge energy at 80 A drops by about 32% relative to that at 25 N.

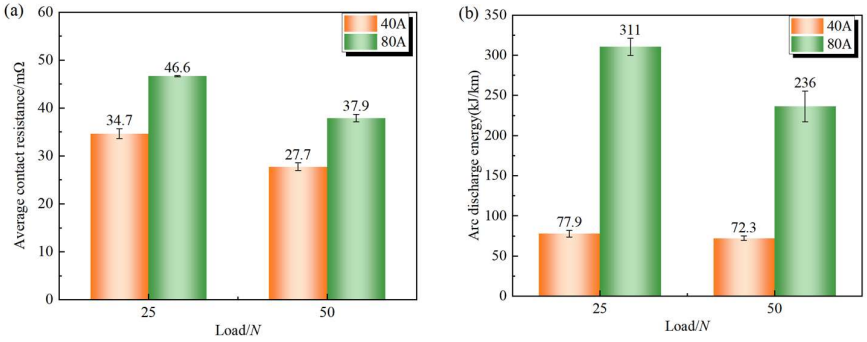


Figure 6. Contact resistance and arc discharge energy under different contact loads. (**a**) Contact resistance; (**b**) arc discharge energy.

3.2. Friction Surface Morphology Analysis

3.2.1. Macroscopic Surface and Three-Dimensional Morphology

Figure 7 shows the macroscopic morphology of the carbon pin surface and the three-dimensional morphology of the wear center region under different contact loads with current intensities of 0 A, 40 A, and 80 A. Under no-current conditions, as the load increased to 50 N, friction marks became more pronounced; the three-dimensional morphology revealed a significant increase in delamination pits and elevated surface roughness. This phenomenon also explains why the friction coefficient at 50 N exceeds that at 25 N under no-current conditions. Under current conditions, when the contact load was 25 N and the current intensity was 40 A, black adhesive deposits were observed on the worn surface of the carbon pin. This is due to the high temperatures generated by the arc discharge during the initial stage of the test, which caused certain substances to leach out from the carbon slip plate [24,25] (as shown in Figure 8). During sustained friction, these substances mixed with abrasive particles and adhered to the contact surfaces. When the current intensity reached 80 A, intense and uneven arc discharges occurred throughout the test, filling the entire contact surface with ablation pits and creating severe surface irregularities. Such roughness reduced the effective contact area, increased contact resistance, and exacerbated localized overheating, forming a vicious cycle. The corresponding three-dimensional morphology data indicate that the surface roughness at 80 A reached 26.7 μm—approximately ten times higher than at 40 A. This indicates that the destructive effect of arc discharge on electrode materials (carbon pins) undergoes a qualitative transformation, evolving from relatively mild wear to a severe, destructive erosion mode. This mode significantly deteriorates the contact performance of friction pairs and accelerates their failure process.

Under a load of 50 N, the wear surface of the carbon pin remains relatively smooth and flat, with no significant ablation marks; mechanical wear continues to dominate as the primary damage mechanism for the friction pair. Specifically, although the friction surface subjected to a current of 40 A is not exposed to high-temperature erosion from arc discharge, Joule heat and frictional heat elevate the contact surface temperature, causing micro-relief features to soften [26] due to heating and thereby reducing the roughness of the friction interface. The corresponding three-dimensional morphology also shows a significant reduction in wear marks on the carbon pin surface, with only a few deep delamination pits remaining. However, when the current increases to 80 A, black ablation regions appear on the wear surface, and the 3D morphology reveals numerous clustered delamination pits

with a markedly higher surface roughness compared to the 40 A condition, confirming that this elevated roughness corresponds to a higher friction coefficient.

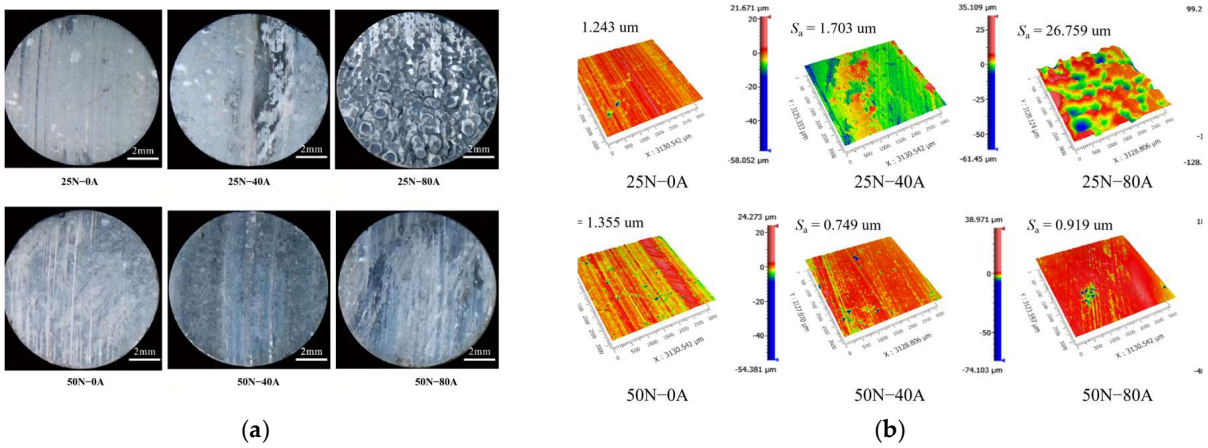


Figure 7. Macroscopic surface and three-dimensional morphology of carbon pin wear. (**a**) Carbon emission reduction at the macro level; (**b**) three-dimensional morphology of the wear area on the carbon damper.

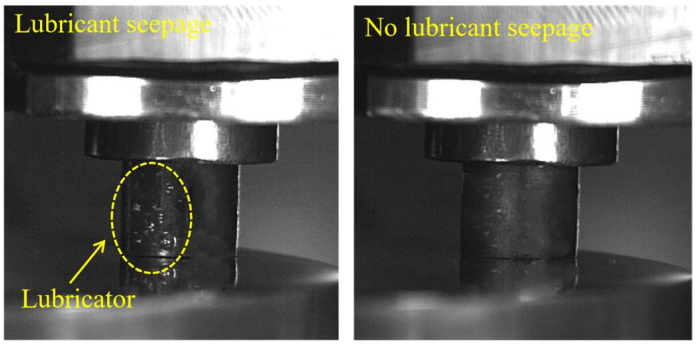


Figure 8. Grease exuded from the carbon pin during the friction process under the 40 A condition.

Figure 9 illustrates the three-dimensional morphology of region 3 on the copper disc's wear surface under varying contact loads. Under non-current-carrying conditions, slight pits appear on the copper disc surface at 50 N, with the surface roughness being slightly higher than at 25 N, indicating that increased contact load under purely mechanical friction enhances compressive stress and shear forces on the surface, leading to plastic deformation, fatigue failure, or minor abrasive wear of localized micro-relief features, thereby exacerbating surface wear damage. Under current-carrying conditions, an increased current magnitude elevates surface roughness as it complicates contact dynamics, causing continuous changes in contact points and a more uneven wear distribution; however, at identical current intensities, higher contact loads actually reduce surface roughness. At low loads, electrical arcs form between contact interfaces during current flow, generating instantaneous high temperatures that induce localized melting, vaporization, or material splashing—where a greater current intensity correlates with a stronger arc intensity and higher temperatures, worsening wear loss. Increased contact load expands the actual contact area between the copper disc and the grinding partner, resulting in more uniform contact point distribution and reduced local current density, thereby mitigating arc-induced damage.

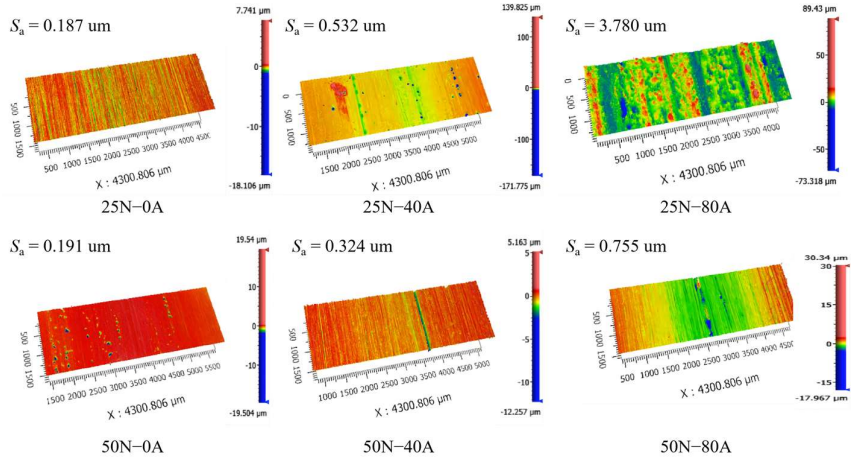


Figure 9. Three-dimensional morphology of the worn surface of the copper disc.

3.2.2. Microscopic Surface Analysis of Carbon Pin

Figure 10 shows the microscopic morphology of the carbon pin surface under no-current conditions with contact loads of 25 N and 50 N, with the inset illustrating the corresponding distribution of copper elements. At a contact load of 25 N, minor spalling pits formed on the pin surface due to mechanical wear (Figure 10(a-1)). Extensive copper deposits are observed around and within these pits. Further analysis reveals that the white flake-like material near the pits consists of copper wear debris transferred from the copper disc during friction (Figure 10(a-2)), predominantly appearing as elongated strips (Figure 10(a-3)). When the contact load increases to 50 N, distinct pitting features emerge on the contact surface; copper deposits are primarily distributed along the sliding friction direction with uneven accumulation patterns (Figure 10(b-1–b-3)). Thus, under non-current conditions, the wear mechanism of the C/Cu contact pair is dominated by abrasive particle wear.

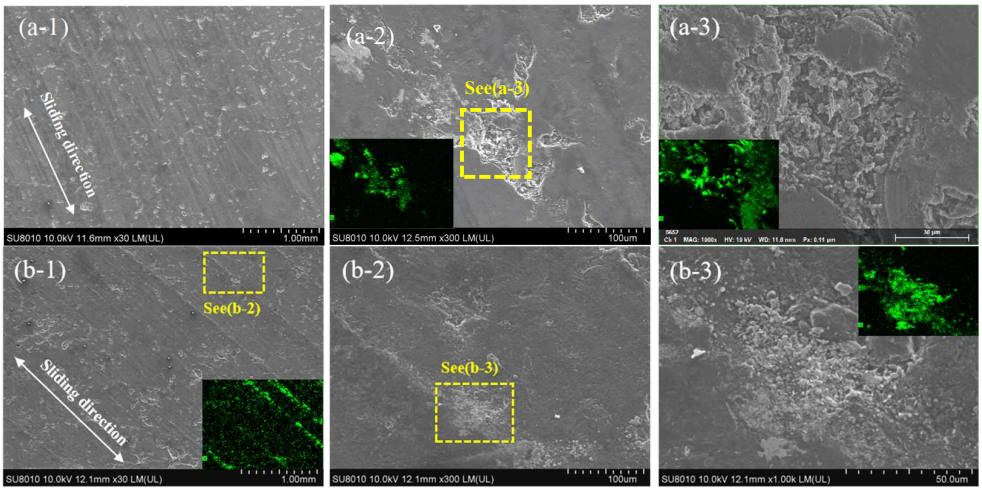


Figure 10. Wear morphology of the carbon pin under the condition of 0 A: (**a-1**) 25 N: a small number of spalling pits have formed on the surface of the carbon pin due to mechanical wear; (**a-2**) 25 N: the material in the spalling pits is copper chips; (**a-3**) 25 N: the copper chips exhibit an elongated strip morphology; (**b-1**) 50 N: grooves have formed on the contact surface of the carbon pin; (**b-2**) 50 N: orientation of copper distribution; (**b-3**) 50 N: copper elements exhibit uneven accumulation.

When the current reaches 40 A, the microstructural morphology of the carbon pin surface under various contact loads and the corresponding copper element distribution are illustrated in Figure 11. Under low-load conditions (Figure 11(a-1)), a strip-shaped arc-

ablated region forms along the sliding friction direction on the pin surface, characterized by a network of loosely structured ablation pits (Figure 11(a-2)). Magnification reveals that this ablation zone exhibits copper enrichment with spherical-shaped particles (Figure 11(a-3)). During friction, copper material undergoes high-temperature erosion from the arc, melts, and splashes onto the pin surface under centrifugal force; subsequent cooling under surface tension causes contraction deformation, forming spherical structures [27,28]. When the contact load increases to 50 N (Figure 11(b-1)), extensive delamination pits appear along the friction direction, revealing significant mechanical damage within these pits (Figure 11(b-2)). Further examination shows that copper material within the ablation pits exists in sheet-like configurations (Figure 11(b-3)). During current-driven friction, thermal concentration softens micro-relief features at the interface. Increased contact load enhances cutting forces between friction pairs [29–31]; when softened micro-reliefs cannot withstand the intensified forces, they undergo delamination and fragmentation.

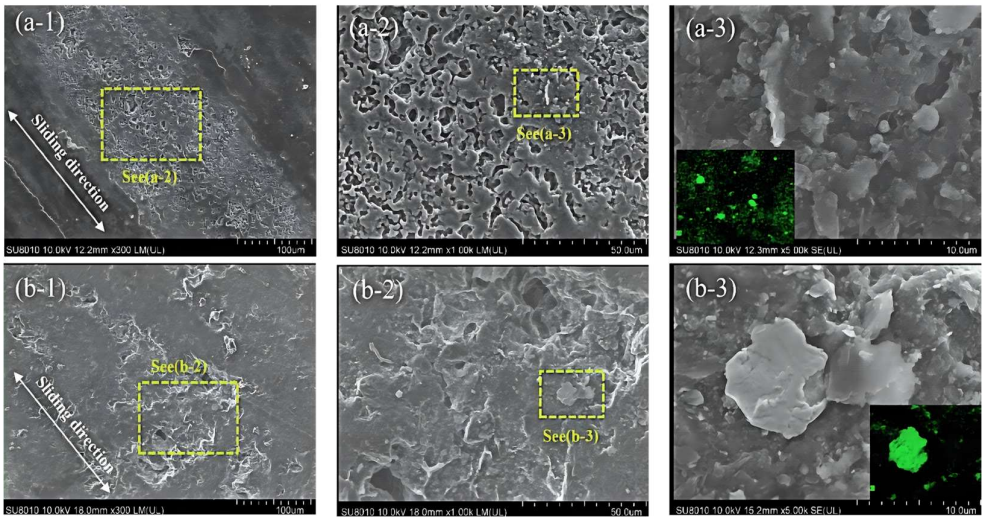


Figure 11. Wear morphology of carbon pin under the condition of 40 A: (**a-1**) 25 N: arc ablation zone; (**a-2**) 25 N: ablation pit; (**a-3**) 25 N: spherical morphology of copper; (**b-1**) 50 N: delamination pit; (**b-2**) 50 N: delamination damage; (**b-3**) 50 N: delamination damage; flaky morphology of copper material.

Figure 12 illustrates the surface morphology and elemental distribution of carbon pins under a current intensity of 80 A with contact loads of 25 N and 50 N. Under low-load conditions (Figure 12(a-1)), the pin surfaces are nearly entirely covered by erosion pits. This occurs because instantaneous temperatures during arc discharge reach approximately 3000–5000 K [32–34], causing carbon to vaporize and sublime, forming ablation pits that significantly degrade the mechanical properties of the surface material. During continuous current-induced friction, micro-relief features on the contact surfaces undergo dynamic changes, resulting in randomly distributed and heterogeneous erosion pits. Additionally, thermal stress cracks and spalling layers form within these pits (Figure 12(a-2)), primarily due to abrupt temperature fluctuations during arc erosion that induce fracture and detachment of surface micro-reliefs, leading to material delamination [35,36]. Figure 12(a-3) clearly shows that the inner walls of erosion pits exhibit a granular structure (Figure 12(a-4)). Surface analysis of this region (Figure 12(a-3)) reveals that the white adherent deposit consists mainly of copper (Cu) and oxygen (O) (Figure 12(a-5)).

When the contact load increases to 50 N, a white film forms on the worn surface of the carbon pin, accompanied by numerous pitting grooves (Figure 12(b-1)). Examination of this white film region under high magnification reveals clusters of adhered white wear debris (Figure 12(b-2)). Element analysis of the area (Figure 12(b-3)) identifies copper and

its oxides as the primary components of the film. Although no electric arc is detected during the friction process under these conditions, the frictional heat generated by sliding friction combined with Joule heating at 80 A accelerates copper oxidation; copper material from the brass disc surface adheres to the carbon pin surface and oxidizes. Under elevated cutting forces, copper is stripped off and deposited on the carbon pin surface in the relative sliding direction, where it compacts to form the white film.

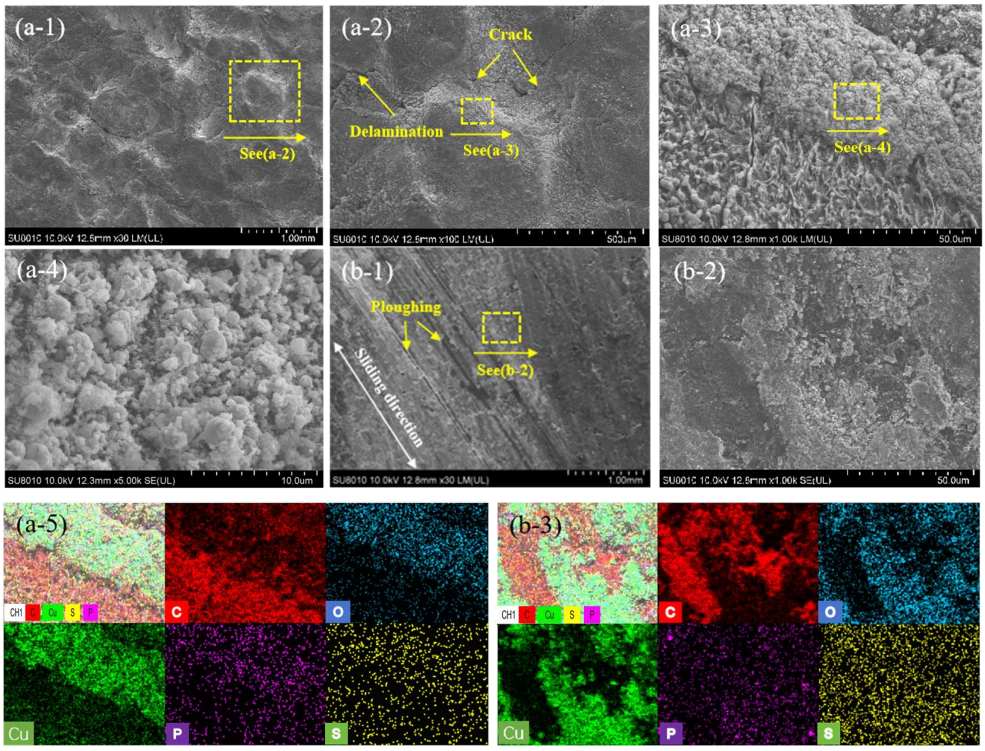


Figure 12. Microscopic surface morphology and element distribution of the 80 A carbon pin under different contact loads: (**a-1**) 25 N: erosion pit; (**a-2**) 25 N: thermal stress cracks and delamination layers within the ablation pit; (**a-3**) 25 N: inner wall of the ablation pit; (**a-4**) 25 N: particulate deposits on the inner wall of the ablation pit; (**a-5**) 25 N: elemental analysis map of the particulate deposits; (**b-1**) 50 N: surface morphology of the carbon pin wear; (**b-2**) 50 N: high-magnification image of the white film region on the carbon pin wear surface; (**b-3**) 50 N: elemental analysis map of the carbon pin wear surface.

4. Discussion

4.1. The Mechanism of Current-Driven Damage and Its Theoretical Significance

The core innovative findings of this study demonstrate that the material damage mechanism undergoes a qualitative transformation with increasing current intensity: under no-current and high-load conditions, material damage primarily manifests as abrasive wear, representing a typical mechanical friction failure; at a 40 A current, mild arc ablation and copper matrix melting and transfer occur on the material surface, with electrical energy beginning to influence the damage evolution process but not playing a dominant role; when the current intensity is increased to 80 A, the material damage enters a severe melting phase, accompanied by the vaporization and sublimation of carbon materials, thermal stress cracking, the formation of delamination pits, and the substantial generation of copper oxides; simultaneously, significant current waveform distortion and "zero-current" characteristics are observed.

The current-induced damage threshold effect described above aligns with existing research findings. Building on this, our study further delineated the critical transition range from "moderate melting transfer" to "destructive melting erosion" and established

corresponding electrical signal criteria: waveform distortion and the "zero-current" phenomenon. From a mechanistic perspective, when the current reaches 80 A, the arc energy density exceeds the sublimation thermal threshold of carbon materials; consequently, the local instantaneous temperature in the friction contact zone can exceed this threshold, causing rapid vaporization of the carbon material. Simultaneously, the thermal shock effect induces significant temperature gradients, triggering microcrack initiation that progressively expands into extensive delamination. The accumulation of copper oxide at the contact interface further degrades its performance, leading to increased contact resistance and ultimately establishing a positive feedback loop for damage progression.

The identification of this damage phase transition point imposes new requirements for developing theoretical models of current-induced friction: while most existing models treat electrical wear as a linear component of mechanical wear, our findings demonstrate that beyond a critical arc energy threshold, damage exhibits nonlinear, abrupt characteristics. Current models must incorporate both arc energy density criteria and material phase transition thresholds to accurately describe damage behavior.

4.2. Research Limitations and Future Directions

This study has elucidated the quantitative relationship between current and load on carbon sliding plates under controlled laboratory conditions; however, several limitations remain. First, the experiment employed copper disc protrusions to simulate uneven contact lines, whose spectral characteristics differ from those of actual contact lines, and did not account for the effects of train speed variations on arc burning frequency or sliding cooling effects—existing research has demonstrated that speed exhibits a turning-point effect on arc burning rate. Additionally, the limited duration of this experiment failed to capture the nonlinear evolution of cumulative damage throughout the entire lifecycle of carbon sliding plates. Future research could focus on two directions: (1) developing a quantitative model linking arc energy with material damage rates by incorporating arc morphology parameters as intermediate variables; (2) conducting multifactorial coupling experiments to investigate the interaction effects of speed, current, and load, with particular attention to the competitive mechanisms between arc cooling and arc enhancement effects under increased speed conditions.

5. Conclusions

This study systematically analyzed the friction and wear performance, electrical contact characteristics, and surface damage mechanisms under arc dominance of carbon/copper contact pairs by simulating arc evolution characteristics under non-uniform contact line conditions and varying current and contact load. The main conclusions are as follows:

(1) The friction coefficient under no-current conditions is significantly higher than that under current-carrying conditions. While increased contact load does not show a positive correlation with the wear rate of the carbon contact pair, the introduction and increase in current substantially exacerbate surface damage in the carbon contact pair.

(2) During current-carrying friction, the arc exhibits distinct morphologies across different cycle stages with significant variations in intensity, typically being most intense during the initial frictional wear phase. Regarding electrical performance, under single-variable conditions, contact resistance is significantly higher at high currents than at low currents, while it is higher under low contact loads than under high contact loads. Furthermore, increasing the contact load improves the contact pair's adhesion and markedly suppresses both arc formation and electrical damage to material surfaces.

(3) The damage mechanism of the material undergoes significant changes with variations in current and load. In the absence of current, under high-load conditions without

arc interference, the material primarily exhibits mechanical wear dominated by abrasive particle wear. Under a current of 40 A, relatively mild arc ablation and copper melting transfer occur on the surface. When the current increases to 80 A, the destructive effect of arc discharge on the material undergoes a qualitative transformation, entering a severe and destructive melting erosion mode; this not only causes significant current waveform distortion and a "zero-current" phenomenon but also leads to carbon vaporization and sublimation at high temperatures, resulting in surface thermal stress cracks, severe spalling pits, and a substantial accumulation of copper oxides.

Author Contributions: Conceptualization, Y.N. and D.J.; methodology, Y.N.; software, Y.N. and W.D.; validation, Y.N., J.S. and L.K.; formal analysis, Y.N.; investigation, Y.N. and L.X.; resources, Y.N.; data curation, Y.N.; writing—original draft, Y.N.; writing—review and editing, Y.N.; supervision, Y.N.; project administration, Y.N.; funding acquisition, Y.N. All authors have read and agreed to the published version of the manuscript.

Funding: This research was funded by the Guangdong Provincial Department of Education's Key Projects in High-End Equipment Manufacturing (Intelligent Robots, New Materials), grant number: 2024ZDZX3089.

Data Availability Statement: The raw data supporting the conclusions of this article will be made available by the authors on request.

Conflicts of Interest: The authors declare no conflict of interest.

References

1. Kaya, M.A.; Yildizli, K.; Ozturk, E.; Dengiz, C.G. The Development of a Mechanical Friction Measurement Approach to Employ a Novel Designed and Manufactured Pantograph Tribometer. *Arab. J. Sci. Eng.* **2026**, *51*, 3621–3648. [CrossRef]
2. Sui, Y.; Xing, P.; Li, G.; Zhang, H.; Wang, W.; Zhang, H. Theoretical Modeling and Numerical Simulation of Current-Carrying Friction and Wear: State of the Art and Challenges. *Lubricants* **2025**, *13*, 370. [CrossRef]
3. Liu, X.-L.; Zheng, Y.-T.; Deng, G.-H.; Xiao, Q.; Shen, M.-X.; Zhang, D.; Cao, H.-Y.; Wang, Z.; Gao, M.-S.; Wu, H.-Y.; et al. Comparative study of the current-carrying property of different copper-impregnated carbon skateboards/contact wires. *Tribol. Int.* **2024**, *195*, 109630. [CrossRef]
4. Liu, X.-L.; Zheng, Y.-T.; Guan, X.; Deng, G.-H.; Xiao, Q.; Gao, M.-S.; Zhang, D.; Cao, H.-Y.; Wang, Z.; Cao, Y.; et al. An investigation revealed the influence of the different magnitude and duration of the current-impact on the wear property to the carbon skateboard/stainless steel contact. *Wear* **2024**, *548–549*, 205366. [CrossRef]
5. Xu, Z.; Gao, G.; Wei, W.; Yang, Z.; Xie, W.; Dong, K.; Ma, Y.; Yang, Y.; Wu, G. Characteristics of pantograph-catenary arc under low air pressure and strong airflow. *High Volt.* **2021**, *7*, 369–381. [CrossRef]
6. Song, Y.; Rønnquist, A.; Jiang, T.; Nåvik, P. Identification of short-wavelength contact wire irregularities in electrified railway pantograph–catenary system. *Mech. Mach. Theory* **2021**, *162*, 104338. [CrossRef]
7. Song, Y.; Antunes, P.; Pombo, J.; Liu, Z. A methodology to study high-speed pantograph-catenary interaction with realistic contact wire irregularities. *Mech. Mach. Theory* **2020**, *152*, 103940. [CrossRef]
8. Luo, Q.; Bruni, S.; Bucca, G.; Mei, G.; Chen, G.; Zhang, W. Wear performance of pantograph-overhead catenary system: A review. *Railw. Eng. Sci.* **2026**, 1–20. [CrossRef]
9. Hu, Y.; Huang, P.; Cheng, C.; Zhang, M.; Ma, R. Influence of arc discharge on the temperature and wear behaviors of the contact strip in pantograph-rigid catenary systems under AC conditions. *Wear* **2024**, *546–547*, 205368. [CrossRef]
10. Yang, H.; Xu, H.; Cai, C.; Deng, X.; Gao, C.; Liu, W.; Ren, W.; Luo, X. Effect of the temperature on the non-uniform wear mechanism of the carbon strip in a pantograph-catenary system with heavy electric current at high speed of 350 km/h. *Proc. Inst. Mech. Eng. Part J. J. Eng. Tribol.* **2026**, *240*, 825–835. [CrossRef]
11. Liu, X.-L.; Zhang, W.-L.; Xiao, Q.; Zhong, Y.; Cao, Y.; Guan, X.; Zhang, S.; Zheng, Y.-T.; Gao, M.-S.; Yang, W.-B.; et al. Study on the effect of different structural parameters on the wear mechanism in the anchor-segment joint of the rigid overhead catenary. *Tribol. Int.* **2024**, *191*, 109108. [CrossRef]
12. Hu, M.-J.; Liu, X.-L.; Zhou, C.-W.; Wang, D.-Y.; Xiao, Q.; Guan, X.; Zhang, S.; Xu, Z.-B. Comparative study of the current-carrying tribological properties of carbon graphite composites with different hardnesses. *Int. J. Mech. Sci.* **2023**, *245*, 108133. [CrossRef]

13. Gao, M.-S.; Liu, X.-L.; Peng, T.; Xiao, Q.; Shen, M.-X.; Zhang, D.; Cao, H.-Y.; Wang, Z.; Yang, W.-B.; Chen, D.-Y. Study on the current-carrying friction and wear behaviors of a novel copper-impregnated carbon skateboard containing tungsten disulfide. *Tribol. Int.* **2025**, *204*, 110430. [CrossRef]
14. Wang, D.; Chen, X.; Li, F.; Chen, W.; Li, H.; Yao, C. Influence of normal load, electric current and sliding speed on tribological performance of electrical contact interface. *Microelectron. Reliab.* **2023**, *142*, 114929. [CrossRef]
15. Zhang, Y.; Li, C.; Pang, X.; Song, C.; Ni, F.; Zhang, Y. Evolution processes of the tribological properties in pantograph/catenary system affected by dynamic contact force during current-carrying sliding. *Wear* **2021**, *477*, 203809. [CrossRef]
16. Sunar, O.; Fletcher, D.; Beagles, A. Laboratory Assessment of ARC Damage in Railway Overhead Contact Lines with a Case Study on Copper-Silver and Low Oxygen Content Copper. *IEEE Trans. Power Deliv.* **2021**, *36*, 3074–3081. [CrossRef]
17. Pan, L.; Yi, X.; Xing, T.; Yu, Z.; Yang, C.; Yu, Q.; Zhu, X.; Zhuang, N.; Jin, A.; Cui, Y.; et al. Arc Erosion Behaviors of Pantograph of High-Speed Train During Its Rise and Fall Processes. *IEEE Access* **2025**, *13*, 165144–165156. [CrossRef]
18. Holey, H.; Sauer, F.; Ganta, P.B.; Mayrhofer, L.; Dienwiebel, M.; Schulze, V.; Moseler, M. Multiscale Parametrization of a Friction Model for Metal Cutting Using Contact Mechanics, Atomistic Simulations, and Experiments. *Tribol. Lett.* **2024**, *72*, 113. [CrossRef]
19. Jackson, R.L.; Crandall, E.R.; Bozack, M.J. An Analysis of Scale Dependent and Quantum Effects on Electrical Contact Resistance Between Rough Surfaces. In Proceedings of the 2012 IEEE 58th Holm Conference on Electrical Contacts, Portland, OR, USA, 23–26 September 2012. [CrossRef]
20. Zhang, Y.; Zhang, C.; Ren, W.; Li, M. Current-dependent Electrical Contact Resistance of connector tip and gold-coated tungsten probe. In *IEEE Transactions on Components, Packaging and Manufacturing Technology*; IEEE: New York, NY, USA, 2026. [CrossRef]
21. Hamedi, M.; Atashparva, M. A review of electrical contact resistance modeling in resistance spot welding. *Weld. World* **2017**, *61*, 269–290. [CrossRef]
22. Cheng, J.; Li, F.; Li, Y.; Wu, H.; Li, B.; Song, C.; Fu, Z.; Zhang, Y. Composite Oxidation Mechanism of Cu/Cu Contact Pairs During Current-Carrying Rolling in O_2-N_2-H_2O Vapor Mixture. *Materials* **2025**, *18*, 5693. [CrossRef]
23. Yang, Z.; Zhao, M.; Wang, X.; Hu, K.; Tian, X.; Zhang, Y. Effect of Normal Load on the Current-Carrying Friction Performance of Copper-10% Graphite Composites. *Coatings* **2025**, *15*, 714. [CrossRef]
24. Ye, J.; Wang, N.; Wu, H.; Wang, C.; Kang, X. Contact Load on the Current-Carrying Tribological Performance of Copper–Graphite Composites. *Materials* **2025**, *18*, 2391. [CrossRef]
25. Yuan, Y.; Wang, L.; Shi, J.; Xia, Y.; Zhou, X.; Liu, J. Mechanisms of interfacial degradation and signal waveform distortion in brush-ring sliding electrical contacts. *Tribol.-Mater. Surf. Interfaces* **2026**, *20*, 145–165. [CrossRef]
26. Yan, X.U. Experimental Study on Friction and Wear Behaviorof Copper-Impregnated Metallized Carbon Strip/Cu-Ag Alloy Contact Wire with Electric Current. *Lubr. Seal.* **2021**, *46*, 34–39. [CrossRef]
27. Zhang, Y.; Zhang, Y.; Song, C. Arc Discharges of a Pure Carbon Strip Affected by Dynamic Contact Force during Current-Carrying Sliding. *Materials* **2018**, *11*, 796. [CrossRef]
28. Günther, I.; Zillmann, B.; Niendorf, T. Metal powder bed fusion of pure and coated copper for power electronics applications using a green laser. *J. Mater. Res. Technol.* **2025**, *38*, 5250–5262. [CrossRef]
29. Wu, G.; Zhou, Y.; Gao, G.; Wu, J.; Wei, W. Arc Erosion Characteristics of Cu-Impregnated Carbon Materials Used for Current Collection in High-Speed Railways. *IEEE Trans. Compon. Packag. Manuf. Technol.* **2018**, *8*, 1014–1023. [CrossRef]
30. Lei, C.; Liang, L.; Jia, L.; Tang, Z.; Xing, Z.; Xie, H.; Zhang, Y.; Lu, Z. Current-carrying wear behavior of QCr0.5/1080 steel friction pair: Multi-physics coupling modeling, experimental validation, and mechanism analysis. *Model. Simul. Mater. Sci. Eng.* **2026**, *34*, 025010. [CrossRef]
31. Yi, F.; Zhong, R.; Zhu, W.; Zhou, R.; Guo, L.; Wang, Y. Comparative Study of Friction Models in High-Speed Machining of Titanium Alloys. *Lubricants* **2025**, *13*, 113. [CrossRef]
32. Deng, C.; Yin, J.; Zhang, H.; Xiong, X.; Wang, P.; Sun, M.; Wu, X. Dynamic variation of arc discharge and its effect on corrosion direction under current-carrying sliding. *Proc. Inst. Mech. Eng. Part J. J. Eng. Tribol.* **2019**, *233*, 380–392. [CrossRef]
33. Wu, S.; Shi, D.; Guo, Y.; Liu, S.; Liu, Q. Gas Temperature Measurement of Low-Current DC Arc in Air by Shadow Imaging. *IEEE Trans. Plasma Sci.* **2025**, *53*, 2342–2350. [CrossRef]
34. Yu, X.; Su, Y.; Song, M.; Yang, J.; Song, L.; Wang, Z.; Liu, Y.; Wei, C.; Cheng, Y. Simulation of Pantograph-Catenary Arc Temperature Field in Urban Railway and Study of Influencing Factors on Arc Temperature. *Infrastructures* **2025**, *10*, 237. [CrossRef]
35. Xiong, X.; Tu, C.; Chen, D.; Zhang, J.; Chen, J. Arc Erosion Wear Characteristics and Mechanisms of Pure Carbon Strip Against Copper Under Arcing Conditions. *Tribol. Lett.* **2014**, *53*, 293–301. [CrossRef]
36. Ji, D.; Mao, F.; Wu, H.; Zhang, Z.; Chen, S.; Wang, J.; Shen, M. From sparks to nanostructures: How arcing induces C/Cu wear and microstructural evolution. *Friction* 2026, *in press*. [CrossRef]

Disclaimer/Publisher's Note: The statements, opinions and data contained in all publications are solely those of the individual author(s) and contributor(s) and not of MDPI and/or the editor(s). MDPI and/or the editor(s) disclaim responsibility for any injury to people or property resulting from any ideas, methods, instructions or products referred to in the content.